Ultrafast acousto-plasmonics in gold nanoparticle superlattices

P. Ruello,[1,*] A. Ayouch,[1] G. Vaudel,[1] T. Pezeril,[1] N. Delorme,[1] S. Sato,[2] K. Kimura,[2,3] and V. E. Gusev[4]

[1]*Institut des Molécules et Matériaux du Mans, UMR-CNRS 6283, Université du Maine, 72085 Le Mans, France*
[2]*School of Science, University of Hyogo, 3-2-1 Koto, Kamigori-cho, Ako-gun, Hyogo 678-1297, Japan*
[3]*Research Center for Micro-Nano Technology, Hosei University, Tokyo, Japan*
[4]*Laboratoire d'Acoustique, UMR CNRS 6613, Université du Maine, 72085 Le Mans, France*

We report the investigation of the generation and detection of GHz coherent acoustic phonons in plasmonic gold nanoparticle superlattices (NPSs). The experiments have been performed with an optical femtosecond pump-probe scheme across the optical plasmon resonance of the superlattice. Our experiments allow us to estimate first the fundamental mechanical parameters such as the collective elastic response (sound velocity) of the NPS and the nanocontact elastic stiffness. Furthermore, it appears that the light-induced coherent acoustic-phonon pulse has a typical in-depth spatial extension of about 45 nm which is roughly four times the optical skin depth in gold. The modeling of the transient optical reflectivity indicates that the mechanism of phonons generation is achieved through ultrafast heating of the NPS assisted by light excitation of the volume plasmon polariton. Based on these results, we demonstrate that it is possible to map the photon-electron-phonon interaction in subwavelength nanostructures which, in particular, provides insights on the fundamental properties of these nanometamaterials.

PACS number(s): 78.67.Pt, 73.20.Mf, 78.47.D−, 62.25.−g

I. INTRODUCTION

Plasmon assisted subwavelength light transmission is a key physical mechanism for modern nano-optics and nano-plasmonics [1]. The propagation of plasmon-polariton waves in nanoparticle nanostructures (chains, arrays) is at the core of intense fundamental investigations and has led to numerous reports [2–6]. For plasmonic applications, it is obviously crucial to understand and control the damping of these plasmon-polariton waves, i.e., the collective propagation distance. This propagation distance as well as a more general description of the dispersion curves for both longitudinal and transverse light electric field have already been obtained for supported one-dimensional (1D) chains [2–5]. The propagation distance is currently limited by the intrinsic electron-phonon, electron-defect interaction within each particle as well as radiation loss. In some particular 2D optical spectroscopy imaging, it has been shown recently that the propagation/distribution of the plasmon polariton could even be mapped for 1D nanoparticles chains [2,6]. The visualization of these plasmons at the interface air/nanostructure with near-field imaging [5] or with an electron-beam imaging [7] were also reported. This state-of-the-art 2D imaging is however limited to 1D or 2D systems, i.e., to surface plasmonics, and no local measurement of volume plasmon-polariton propagation has been reported for 3D nanoparticles arrays so far. Most of the plasmonic responses in nanoparticle superlattices are obtained indeed from far-field optical absorbance measurements [8,9]. Because of the difficulty to probe the inner part of a plasmonic superlattice, no quantitative depth profiling description of the plasmon-polariton propagation has been reported to date. However, it is known that ultrafast optical techniques can provide a picture in time and space of the light-matter interaction [10–12]. In particular, in the case of femtosecond light pulses, the light-matter coupling can lead to the emission of coherent acoustic phonons that occurs all over the spatial extension where the light energy is converted into mechanical energy. Consequently, the characteristic spatial profile of the emitted coherent acoustic phonons contains information on the light-matter energy conversion process. In bulk solids, the analysis of the coherent acoustic-phonon packet has permitted to understand the evolution in time and in space of the different electron-acoustic-phonon interactions like the thermoelastic process (ultrafast heating of the lattice) [13–15], the deformation potential process (electronic pressure) [16–18], and even, reported recently, the spatial electron-hole separation in semiconductors (i.e., the photoinduced Dember electric field) [19].

In this paper, by applying the optical pump-probe scheme depicted in Fig. 1, we report the observation of GHz coherent acoustic-phonon generation in plasmonic nanoparticle super-lattices (NPSs). The laser excited coherent acoustic pulse has a spatial extension in the range of 45 nm which is much larger than either the gold nanoparticle diameter (3.7 nm) or the light penetration depth in gold. Because laser-excited hot electrons are confined in the gold nanoparticles, these observations indicate that the acoustic phonons are very likely induced by ultrafast heating of the superlattice assisted by a collective plasmon-polariton propagation. Moreover, while individual vibrations in nanoparticle assemblies [20,21] or narrow-band Brillouin mode in semitransparent cobalt superlattice [22] have been reported earlier, our results demonstrate that it is possible to generate propagating broadband coherent acoustic phonons in plasmonic NPSs. We are then able to estimate the sound velocity in these superlattices over a frequency range of 5–30 GHz and hence to evaluate the nanocontact elastic stiffness. Both these parameters are crucial for understanding the thermal properties of these artificial nanometric lattices.

Besides these findings, we believe that this approach could be used in a broader range of nanophotonics and nanoplasmonics where it is crucial to understand how light penetrates in complex nanomaterials and metamaterials within which propagation of light can be unusual with negative

_____
*pascal.ruello@univ-lemans.fr
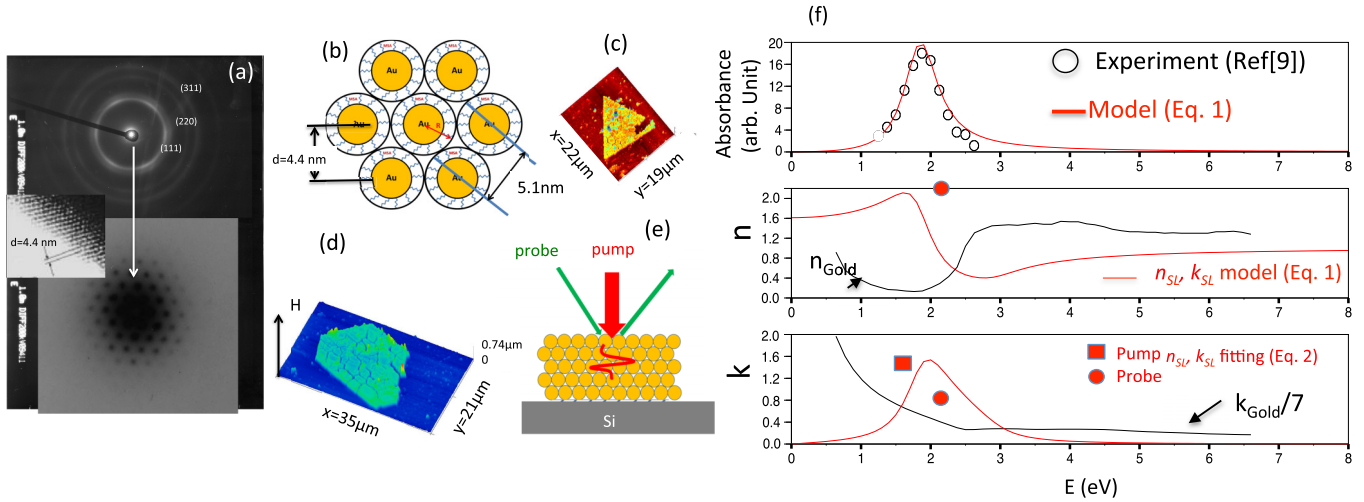
FIG. 1. (Color online) (a) Transmission electron diffraction (TED) pattern showing the Debye Scherrer rings (top figure) coming from the crystallized cubic gold nanoparticles. In the middle figure, the transmission electron microscopy image (TEM) shows the mesoscopic hexagonal arrangement (hcp) with the two neighbor plane distance of 4.4 nm. The hcp arrangement is also well evidenced with small angle electron diffraction revealing the 6-fold axis (bottom figure). (b) Sketch of the gold nanoparticle superlattices connected via mercaptosuccinic acid (MSA) molecules. (c) Optical microscopy view of a superlattice deposited onto a silicon substrate. (d) Atomic force microscopy (AFM) profile of the hexagonal shape superlattice (height $H = 180$ nm). (e) Sketch of the pump and probe experiments performed on these nanoparticle superlattice where coherent acoustic phonons are generated and detected in the front-front configuration. (f) Top panel: plasmon resonance of the gold superlattice from [9] fitted with Eq. (1). Middle and bottom panels: refractive index (real n and imaginary parts k) of the gold superlattice compared to those of bulk gold [31]. The red symbols (square and circles) are the refractive index values estimated with the photoacoustic response [see Eq. (2) and details in the text].

refractive index, for example [23,24]. This technique (i.e., of the detection and analysis of the acoustic pulse profile) could also be potentially applied to measure light attenuation in materials and for the depth profiling of the materials with in-depth inhomogeneity modulating the efficiency of the opto-acoustic conversion as it is currently widely used in biomedical imaging [25,26].

II. RESULTS AND DISCUSSION

The samples have been grown by soft chemical routes (for ample details see the review [27]). These nanoparticles, encapsulated with 0.7-nm-long molecular chains (MSA Mercaptosuccinic), are packed on a silicon substrate according to a hexagonal structure (hcp packing) with the c axis perpendicular to the substrate [the sixfold symmetries are clearly visible in Figs. 1(a), 1(c), and 1(d) from nanometric to micrometric scales]. The measured NPS spacing of $d = 5.1$ nm gives the particle diameter of 3.7 nm. Two different superlattices have been studied with typical lateral size of tens of micrometers and a thickness of 52 nm [triangular shape, Fig. 1(c)] and 180 nm [hexagonal shape, Fig. 1(d)]. These ordered assemblies exhibit plasmonic properties [Fig. 1(f)] with a collective response modeled with the following simple phenomenological dielectric function [28,29]:

$$\epsilon_{SL}(\omega) = 1 + \frac{\omega_P^2}{\omega_S^2 - \omega_P^2/3 - \omega^2 - i\Gamma\omega}. \tag{1}$$

The real (n_{SL}) and imaginary (k_{SL}) parts of the refractive index, as well as the plasmon dielectric losses ($\propto 2nk\omega$ [30]), have been deduced from this dielectric function ($\tilde{n}_{SL} = n_{SL} + ik_{SL} = \sqrt{\epsilon_{SL}}$) and are shown in Fig. 1(f) where $\omega_S =$

2.3 eV, $\omega_P = 2.2$ eV and $\hbar\Gamma = 0.59$ eV. As originally defined [28], ω_P is the effective collective plasmon energy. It has the usual form known for the Sommerfeld model of metals [30] with $\omega_P = Ne^2/m\epsilon_0$, but here, N is the number per unit volume of plasmonic gold nanoparticles (and not the electron concentration as in the Sommerfeld model) and m is the mass of a single plasmonic gold nanoparticle. The individual nanoparticle (i.e., individual resonator) has its own plasmon energy which is ω_S (ϵ_0 is the dielectric constant in vacuum). The last term $\hbar\Gamma$ is the damping energy of the collective effective volume plasmon mode. The resonance shift term ($\omega_S^2 - \omega_P^2/3$) arises from the mutual interaction between neighbor nanoparticles in the effective model approach [28]. The effective dielectric constants of the gold nanoparticles superlattice are shown in Fig. 1(f) (see middle and bottom panels) where one can notice that both the real and imaginary parts are clearly different from those of bulk gold crystal [31]. By comparing this model and more recent numerical calculations [32], we can notice that Eq. (1) gives a reasonable approximation for very small nanoparticles (for instance 3.7 nm) while it does not work anymore for larger nanoparticles diameter (>20 nm).

The pump-probe technique used here is based on an 80-MHz repetition rate Ti:sapphire femtosecond laser. The beam is split with a polarizing beam splitter into pump and probe beams. The probe beam is introduced in a synchronously pumped optical parametric oscillator (OPO) that allows us to tune the wavelength and permit us to perform two-color pump-probe experiments (the pump and probe are linearly and circularly polarized respectively). The transient optical reflectivity signals are obtained thanks to a mechanical delay stage (delay line) which enables a controlled arrival time of
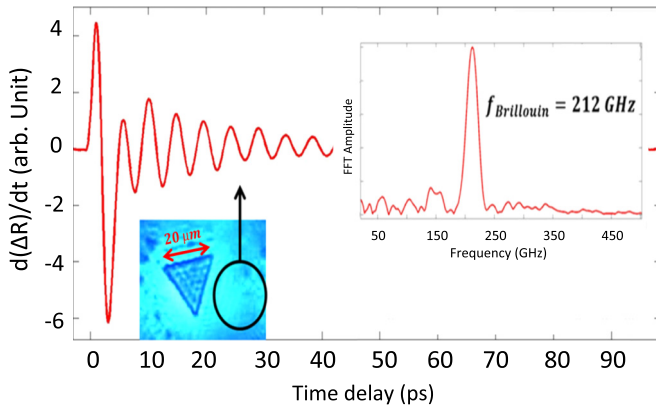
FIG. 2. (Color online) Coherent acoustic phonons generated and detected in the silicon substrate only revealing the expected coherent acoustic-phonon Brillouin mode at 212 GHz (pump at 1.49 eV, probe at 2.99 eV).

the probe pulse regarding to the arrival of the pump pulse. The experiments were conducted with incident pump and probe beams perpendicular to the surface of the nanoparticle superlattice as shown in Fig. 1(e) with a typical pump and probe spot diameter of 5 μm which is roughly three times smaller than the typical lateral size of the superlattice crystal.

The first signal shown in Fig. 2 is the one obtained when the pump and probe beams are focused only on the silicon substrate. The signal contains an oscillating component with a frequency of 212 GHz. This mode is the well-known coherent acoustic-phonon signal detected in silicon. In particular, this mode is the Brillouin mode in (111) silicon whose frequency is given by $f_{Si} = 2n_{Si}V_{Si}/\lambda = 220$ GHz, where $n_{Si} = 5$ is the refractive index of silicon at the probe energy 2.99 eV and $V_{Si} = 9400$ m s^{-1} is the longitudinal sound velocity in Si(111). When the pump beam is focused on the nanoparticle superlattice, the transient optical reflectivity signals obtained for the superlattice are very different as shown in Figs. 3 and 4. Time-resolved reflectivity signals have been recorded for variable probe wavelengths (2.17–2.25 eV) but no significant variation have been observed in this wavelength range, probably because of the broad collective plasmon resonance [Fig. 1(f)].

For the thicker NPS of 180 nm, the transient optical reflectivity signal exhibits oscillatory components up to nearly 1 ns (pump 1.59 eV, probe 2.19 eV). In order to better reveal the oscillatory parts of the signal we processed the numerical time derivative shown in Fig. 3(a). At first glance, the observation of the signal in the time domain reveals some periodic bursts repeated about every 200 ps [Fig. 3(a)]. We attribute this to an acoustic pulse laser-generated at the NPS free surface and traveling back and forth across the NPS and periodically detected at the front side upon reflection at the Si substrate interface. This interpretation is confirmed from the analysis of the FFT signals [Fig. 3(b)] where the detected frequencies follow the expected eigenmodes frequency sequence $f_n = nV_{LA}/2H$, with $n = 1, 2, 3..., V_{LA}$ is the longitudinal sound velocity, and H is the NPS thickness [see inset of Fig. 3(b)]. From the mean least-square analysis of the slope, we extract a sound velocity of $V_{LA} = 1770$ m s^{-1}
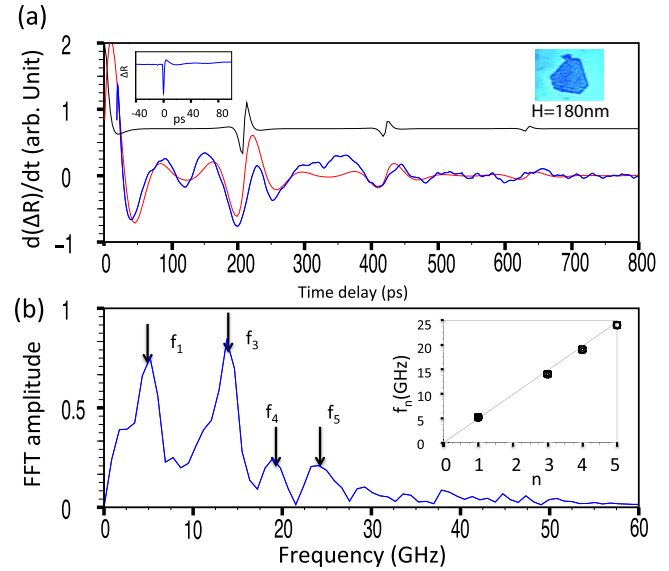
FIG. 3. (Color online) (a) Time derivative of transient optical reflectivity revealing the coherent acoustic-phonon signal (blue curve) with numerical adjustment (red curve) containing information on the acousto-plasmonic processes of the generation and detection of the acoustic phonons [see Eq. (2)] (inset shows the fast electronic response of the superlattice). As a comparison a simulation of the coherent acoustic-phonon signal is given when the pump light energy is converted only within the gold crystal skin depth (i.e., 11 nm at 1.59 eV without hot electrons diffusion) and probed with standard optical properties of gold crystal (black curve). (b) Corresponding coherent acoustic-phonon spectrum obtained by a fast Fourier transform (FFT) of the experimental time derivative transient signal shown in (a). Four harmonics of the mechanical resonance of the superlattice appear (inset).

which is about half of that measured in bare gold crystals. The decrease of the sound velocity is an indication of the soft nanocontacts between nanoparticles. The time derivative signal shown in Fig. 4(a) corresponding to the thinnest NPS
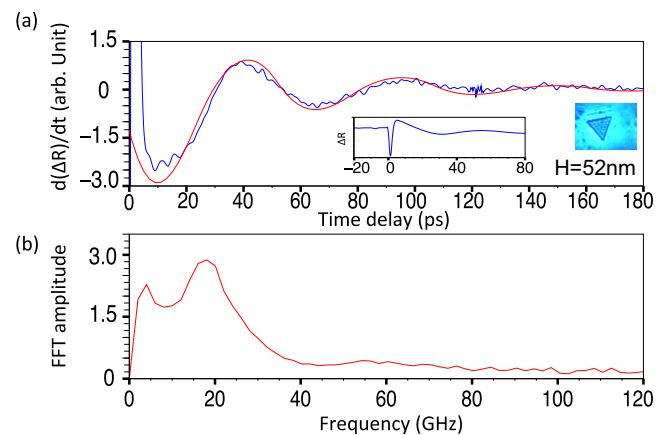
FIG. 4. (Color online) (a) Time derivative of transient optical reflectivity revealing the coherent acoustic-phonon signal (blue curve) with numerical adjustment with a damped sinus (red curve) (inset shows the fast electronic response of the superlattice). (b) Corresponding coherent acoustic-phonon spectrum obtained by a fast Fourier transform (FFT) of the experimental time derivative transient signal shown in (a).

of 52 nm thickness resembles a damped sinus function of about 18–19-GHz fitted frequency [Fig. 4(b)]. This mode is the first mechanical resonance (f_1) of the entire superlattice which is usually predominantly excited when the layer is thin enough as already observed in different nanometric thin films [33–35]. This mechanical resonance first harmonic leads to the estimate of $V_{LA} \approx$ 1870–1970 m s^{-1}, in close agreement with the previous estimate obtained for the thicker superlattice. The estimate of the bulk sound velocity offers a unique way to evaluate precisely, without contact methods, a fundamental mechanical parameter such as the molecular contact elastic stiffness between nanoparticles. Following the hcp lattice dynamic equation along the z axis, we can connect the sound velocity to that nanoparticle contact effective stiffness K with $V_{LA} = (4/\sqrt{3})d\sqrt{K/m}$ [36] where $d = 5.1$ nm is the interparticle distance. With a particle diameter of 3.7 nm the mass becomes $m = 5.1 \times 10^{-22}$ kg, leading to $K \approx 11$ N m^{-1} consistently with covalent bonds and stronger than van der Waals connection probed in soft assemblies of nanoparticles [21,34].

Besides the evaluation of collective sound velocity and the nanocontact stiffness, the analysis of the coherent acoustic-phonon spectrum provides insights on the ultrafast generation processes, i.e., on the coupling between photon, electron, and phonon. The transient optical signal reported for the thicker superlattice is clearly different from those obtained earlier for films made of noble metals like gold, silver [14], or copper [15]. The physical characteristics of the photogeneration and photodetection processes can be obtained thanks to a proper analysis and simulation of the transient reflectivity signal ($\Delta R/R$). We performed this simulation for the thicker superlattice only since we have a richer acoustic-phonon spectrum that provides better accuracy. For that, we employed the standard transient reflectivity model where in our case $\Delta R/R = 2\text{Re}(\delta r/r)$ with [10,37–39]

$$\delta r/r \simeq \rho + i\delta\phi \simeq -2ik_0\delta z$$
$$+ \frac{4ik_0\tilde{n}_{SL}}{(1-\tilde{n}_{SL}^2)}\frac{d\tilde{n}_{SL}}{d\eta}\int_0^\infty \eta(z,t)\exp(2ik_0\tilde{n}_{SL}z)dz, \quad (2)$$

where $k_0 = 2\pi/\lambda$ is the probe wave vector in air, $\eta(z,t)$ is the coherent acoustic-phonon strain field propagating perpendicularly to the surface of the sample, and $d\tilde{n}_{SL}/d\eta$ is the photoelastic coefficient. $z = 0$ corresponds to the air/superlattice interface. In Eq. (2), the first term corresponds to the contribution of the surface displacement (δz) of the superlattice at $z = 0$ [see coordinates in Fig. 5(b)]. The second term of Eq. (2) is the photoelastic contribution (due to the modification of the refractive index of the superlattice induced by the strain field of the coherent acoustic phonons). The strain field has been modeled by applying the standard bipolar shape [10] with $\eta(z,t) = -\text{sgn}(z - V_s t)\exp(-|z - V_s t|/\xi)$. The simulation of the photoinduced strain $\eta(z,t)$ is shown as a dotted curve in the inset of Fig. 5(a) where ξ is the characteristic depth over which the photoinduced strain occurs. ξ is related to the apparent imaginary part of the refractive index k_{SL}^{pump} at the pump wavelength with $\xi = \lambda/4\pi k_{SL}^{pump}$. In order to take into account phonon attenuation (anharmonic damping, defect scattering), we have used a cutoff frequency at around 30 GHz [full line curves in Fig. 5(a) and in
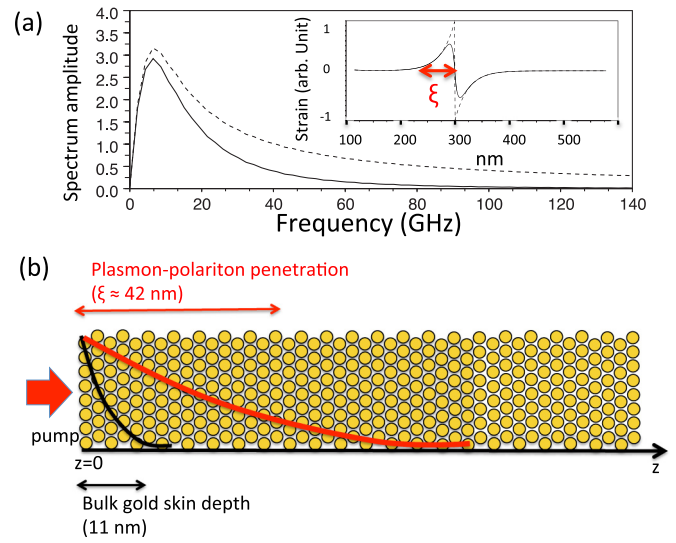
FIG. 5. (Color online) (a) The full (dotted) line curve represents the photoinduced coherent acoustic-phonon spectrum with (without) phonon attenuation used to adjust the transient photo-acoustic response shown in Fig. 3(b). The inset shows the emitted coherent acoustic-phonon strain (ultrafast heating of nanoparticles) with a spatial extension of 42 nm used for the simulation. This spatial extension is sketched by the red curve in (b) where it is compared to the penetration depth of light into bulk gold.

inset of Fig. 5(a)] in accordance with the experimental FFT [Fig. 3(b)]. The calculation takes into account the reflection of the acoustic-phonon wave packet at the silicon interface to reproduce the three visible acoustic echoes. The best adjusted parameters we have obtained concerning the probe optical properties (at 2.19 eV) are $\tilde{n}_{SL}^{probe} = 2.2 + 0.9i$ and for the pump (at 1.59 eV) $k_{SL}^{pump} = 1.5$. These optical coefficients are plotted as a red square and circle in Fig. 1(f) and the fitted curve of the time derivative $d(\Delta R/R)/dt$ compared to the experimental data is shown in Fig. 3(a). The adjustment of the shape of the photo-acoustic signal depends also on the photoelastic coefficient $d\tilde{n}_{SL}/d\eta$ [10] which is unknown for such artificial nanoparticle superlattices. However we have tested different scenarios and our adjustment shows that the real part of the photoelastic coefficient is dominant over its imaginary part. Considering the well-known relationship $d\tilde{n}_{SL}/d\eta \propto d\tilde{n}_{SL}/dE$ [10], E being the probe energy, and from the energy dependence of the NPS refractive index shown in Fig. 1(f), it appears that the derivative of the real part (n_{SL}) (in particular at 2.19 eV) is much larger than that of the imaginary part (k_{SL}). Consequently and in accordance with our simulations, it indicates that the real part of the photoelastic coefficient may dominate with $d\tilde{n}_{SL}/d\eta \sim dn_{SL}/d\eta$.

The results of our simulations confirm that the optical properties of the NPSs are deeply different than those of bulk gold crystal. As a comparison, we have performed as well a calculation where we simulate the transient optical signal considering that the photoinduced strain occurs over a depth of 11 nm beneath the surface, as in bare gold metal as sketched in Fig. 5(b) (hot electron diffusion is neglected). The simulation is shown in Fig. 3(a) (black curve) obtained with an optical refractive index for gold (at 2.19 eV)

$\tilde{n}_{Au} = 0.25 + 3i$ and (at 1.59 eV) $\tilde{n}_{Au} = 0.3 + 6i$ [31]. The discrepancy between this simulation (black curve) and our experimental result (red and blue curves) clearly confirms that the photoinduced acoustic pulse in the plasmonic superlattice is much broader than that expected when pump light interacts with bare gold only over the skin depth. This straightforwardly demonstrates that the pump light can deeply penetrate this subwavelength plasmonic nanostructure over a distance of about $\xi \sim 42$ nm, much larger than the optical penetration depth of bare gold. Furthermore, this distance over which the conversion of light energy into mechanical energy occurs is not compatible with transport of hot electrons due to the existence of insulating contacts between the nanoparticles as already discussed in a previous work [29]. As a consequence, the ultrafast generation of coherent acoustic phonons in our NPS can only be interpreted from an ultrafast heating of the NPS assisted by transport of the electromagnetic energy through plasmon-polariton propagation perpendicular to the surface. This plasmon-polariton propagation perpendicular to the surface might be associated to first neighbors dipolar and quadrupolar electromagnetic interactions whose detailed mechanisms need further modeling by now.

As a summary, we have demonstrated the generation and detection of coherent acoustic phonons in gold nanoparticle superlattices. The analysis of the GHz sound propagation has permitted us to estimate the fundamental mechanical parameter that is the nanocontact stiffness. Furthermore, our results demonstrate that the emission of coherent acoustic phonons occurs in the NPS over a distance of about 45 nm which is much larger than the skin depth in gold as well as much larger than a single gold nanoparticle diameter. As a matter of fact, the observed spatial spreading of the conversion of light energy into mechanical energy requires transportation of the light energy in the subwavelength regime. We attribute this effect to an ultrafast heating assisted by plasmon-polariton propagation perpendicular to the NPS surface. The model of the generation and detection of coherent acoustic phonons is consistent with this mechanism. These results open interesting perspectives for the manipulation of plasmons by coherent phonons or vice versa as recently investigated both theoretically and experimentally [40,41]. Moreover, this acousto-plasmonics approach is an alternative and complementary method for mapping the photon-electron-phonon interaction at the nanoscale which is still a matter of many developments [2–7,23,24].

[1] W. L. Barnes, A. Dereux, and T. W. Ebbesen, Nature (London) **424**, 824 (2003).

[2] D. Solis, Jr., B. Willingham, S. L. Nauert, L. S. Slaughter, J. Olson, P. Swanglap, A. Paul, W.-S. Chang, and S. Link, Nano Lett. **12**, 1349 (2012).

[3] M. L. Brongersma, J. W. Hartman, and H. A. Atwater, Phys. Rev. B **62**, R16356 (2000).

[4] S. A. Maier, M. L. Brongersma, P. G. Kik, and H. A. Atwater, Phys. Rev. B **65**, 193408 (2002).

[5] S. A. Maier, P. G. Kik, H. A. Atwater, S. Meltzer, E. Harel, B. E. Koel, and A. A. G. Requicha, Nat. Mater. **2**, 229 (2003).

[6] A. Teulle, M. Bosman, C. Girard, K. L. Gurunatha, M. Li, S. Mann, and E. Dujardin, Nat. Mater. **14**, 87 (2015).

[7] M. Bosman, V. J. Keast, M. Watanabe, A. I. Maaroof, and M. B. Cortie, Nanotechnology **18**, 165505 (2007).

[8] A. R. Tao, D. P. Ceperley, P. I. Sinsermsuksakul, A. R. Neureuther, and P. Yang, Nanoletters **8**, 4033 (2008).

[9] T. Oonishi, S. Sato, H. Yao, and K. Kimura, J. Appl. Phys. **101**, 114314 (2007).

[10] C. Thomsen, H. T. Grahn, H. J. Maris, and J. Tauc, Phys. Rev. B **34**, 4129 (1986).

[11] V. Gusev and A. Karabutov, *Laser Optoacoustics* (AIP, New York, 1993).

[12] P. Ruello and V. Gusev, Ultrasonics **56**, 21 (2015).

[13] G. Tas and H. J. Maris, Phys. Rev. B **49**, 15046 (1994).

[14] O. B. Wright, Phys. Rev. B **49**, 9985 (1994).

[15] M. Lejman, V. Shalagatskyi, O. Kovalenko, T. Pezeril, V. V. Temnov, and P. Ruello, J. Opt. Soc. Am. B **31**, 282 (2014).

[16] N. V. Chigarev, D. Yu. Paraschuk, X. Y. Pan, and V. E. Gusev, Phys. Rev. B **61**, 15837 (2000).

[17] O. B. Wright, B. Perrin, O. Matsuda, and V. E. Gusev, Phys. Rev. B **64**, 081202(R) (2001).

[18] E. S. K. Young, A. V. Akimov, R. P. Campion, A. J. Kent, and V. Gusev, Phys. Rev. B **86**, 155207 (2012).

[19] G. Vaudel, T. Pezeril, A. Lomonosov, M. Lejman, P. Ruello, and V. Gusev, Phys. Rev. B **90**, 014302 (2014).

[20] I. Lisiecki, V. Halte, C. Petit, M.-P. Pileni, and J.-Y. Bigot, Adv. Mater. **20**, 4176 (2008).

[21] P. A. Mante, H.-Y. Chen, M.-H. Lin, Y.-C. Wen, S. Gwo, and C.-K. Sun, Appl. Phys. Lett. **101**, 101903 (2012).

[22] I. Lisiecki, D. Polli, C. Yan, G. Soavi, E. Duval, G. Cerullo, M.-P. Pileni, Nano Lett. **13**, 4914 (2013).

[23] K. L. Tsakmakidis, A. D. Boardman, and O. Hess, Nature (London) **450**, 397 (2007).

[24] A. Govyadinov, *Light Propagation in Nanostructured Metamaterials and Micro-Resonators: Subwavelength Light Confinement and Quantum Chaos*, (VDM Verlag, 2010).

[25] L. H. Wang and H. I. Wu, *Biomedical Optics* (Wiley, New York, 2007)

[26] M. Xu and L. V. Wang, Rev. Sci. Instrum. **77**, 041101 (2006).

[27] H. Yao, S. Sato, and K. Kimura, in *Nanoparticle Assemblies and Superstructures*, edited by N. Kotov (Taylor & Francis, Boca Raton, 2005), pp. 601–614.

[28] P. A. Cox, *The Electronic Structure and Chemistry of Solids* (Oxford University Press, Oxford, 1987), Chap. 2.

[29] S. Sato, H. Yao, and K. Kimura, Chem. Lett. **31**, 526 (2002).

[30] J. M. Ziman, *Principle of Theory of Solids* (Cambridge University Press, Cambridge, England, 1964).

[31] P. B. Johnson and R. W. Christy, Phys. Rev. B **6**, 4370 (1972).

[32] H. Alaeian and J. A. Dionne, Opt. Express **20**, 15781 (2012).

[33] C. Mechri, P. Ruello, and V. Gusev, New J. Phys. **14**, 023048 (2012).

[34] A. Ayouch, X. Dieudonne, G. Vaudel, H. Piombini, K. Valle, V. Gusev, P. Belleville, and P. Ruello, ACS Nano **6**, 10614 (2012).

[35] T. Pezeril, F. Leon, D. Chateigner, S. Kooi, and K. A. Nelson, Appl. Phys. Lett. **92**, 061908 (2008).

[36] A. Merkel, V. Tournat, and V. Gusev, Phys. Rev. E **82**, 031305 (2010).

[37] V. E. Gusev, Acust. Acta Acust. **82**, S37 (1996).

[38] B. Perrin, B. Bonello, J.-C. Jeannet, and E. Romatet, Prog. Nat. Sci. **6**, 444 (1996).

[39] O. Matsuda, M.-C. Larciprete, R. Li Voti, and O. B. Wright, Ultrasonics **56**, 3 (2015).

[40] K. O'Brien, N. D. Lanzillotti-Kimura, J. Rho, H. Suchowski, X. Yin, and X. Zhang, Nat. Commun. **5**, 4042 (2014).

[41] V. V. Temnov, Nat. Photon. **6**, 728 (2012).